Research Article

ADVANCED PHOTONICS

Gradient defects mediate negative thermal quenching in phosphors

Mingxue Deng,[a,b,†] Xingzhong Cao,[c,†] Yangmin Tang,[a,b] Zhenzhen Zhou,[a,*] Lijia Liu,[d] Xiaofeng Liu,[e] Peng Zhang,[c] Lo-Yueh Chang,[f] Hao Ruan,[g] Xinjun Guo,[g] Jiacheng Wang,[a,b,h,i,*] and Qian Liu[a,b,*]

[a]Chinese Academy of Sciences, Shanghai Institute of Ceramics, State Key Laboratory of High Performance Ceramics and Superfine Microstructure, Shanghai, China
[b]University of Chinese Academy of Sciences, Center of Materials Science and Optoelectronics Engineering, Beijing, China
[c]Chinese Academy of Sciences, Institute of High Energy Physics, Beijing, China
[d]Western University, Department of Chemistry, London, Ontario, Canada
[e]Zhejiang University, School of Materials Science and Engineering, Hangzhou, China
[f]National Synchrotron Radiation Centre, Hsinchu, Taiwan
[g]Chinese Academy of Sciences, Shanghai Institute of Optics and Fine Mechanics, Laboratory of Micro-Nano Optoelectronic Materials and Devices, Shanghai, China
[h]North China University of Science and Technology, College of Materials Science and Engineering, Hebei Provincial Key Laboratory of Inorganic Nonmetallic Materials, Tangshan, China
[i]Taizhou University, School of Materials Science and Engineering, Taizhou, China

Abstract. Luminescent materials often suffer from thermal quenching (TQ), limiting the continuation of their applications under high temperatures up to 473 K. The formation of defect levels could suppress TQ, but rational synthesis and deep understanding of multiple defects-regulated luminescent materials working in such a wide temperature range still remain challenging. Here, we prepare a negative thermal quenching (NTQ) phosphor $LiTaO_3:Tb^{3+}$ by introducing gradient defects V_{Ta}^{5-}, Tb_{Li}^{2+}, and $(V_{Ta}Tb_{Li})^{3-}$ as identified by advanced experimental and theoretical studies. Its photoluminescence significantly becomes intense with rising temperatures and then slowly increases at 373 to 473 K. The mechanism studies reveal that gradient defects with varied trapping depths could act as energy buffer layers to effectively capture the carriers. Under thermal disturbance, the stored carriers could successively migrate to the activators in consecutive and wide temperature zones, compensating for TQ to enhance luminescence emission. This study initiates the synthesis of multi-defect NTQ phosphors for temperature-dependent applications.

Keywords: gradient defects; negative thermal quenching; energy buffer layers; temperature-dependent information encryption.

Received Nov. 9, 2022; revised manuscript received Dec. 28, 2022; accepted for publication Jan. 19, 2023; published online Feb. 14, 2023.

[DOI: 10.1117/1.AP.5.2.026001]

1 Introduction

Luminescent materials show wide-ranging application prospects in light-emitting devices,[1–4] anti-counterfeiting,[5,6] biological imaging,[7,8] and optical information storage.[9] However, the emission intensity of most luminescent materials is evidently reduced under the temperature range of 373 to 473 K compared to the initial state, which greatly limits their applications under high temperatures up to 473 K. The emission loss with increasing temperature is known as the thermal quenching (TQ) effect,[10–12] one of the greatest obstacles to extend the commercial applications of existing materials.[13–15] The TQ results in significant increase of non-radiation distribution of excited state electrons of luminescent ions. Therefore, it is urgent to explore anti-TQ luminescent materials from theoretical principles as well as rational design, which could show stable or enhanced emission with increasing temperature up to 473 K.

Rational introduction and regulation of defect levels in materials have been regarded as an effective strategy to suppress

*Address all correspondence to Zhenzhen Zhou, zhouzhenzhen@mail.sic.ac.cn; Jiacheng Wang, jiacheng.wang@mail.sic.ac.cn; Qian Liu, qianliu@mail.sic.ac.cn
†These authors contributed equally to this work.

the TQ effect, resulting in zero TQ or even negative TQ (NTQ).[13,16–18] The NTQ effect means thermally enhanced emission with increasing temperatures, allowing for obtaining higher-intensity lighting of phosphors compared to that at room temperature (RT). Gradient defects in phosphors mainly include vacancies (e.g., cationic vacancy, oxygen vacancy) and aliovalent substitutions. Xia et al. reported an aliovalent substituting strategy to realize multimode deep-ultraviolet emission in in trap-mediated host lattice Li_2CaGeO_4.[19] Under increasing temperatures, the charge carriers stored in the defects could be thermally released and transferred to the luminescence centers, thus compensating for the emission loss due to nonradiative transition.[20,21] Kim et al. reported a cation vacancy-induced phase transition with energy transfer (ET) from the defect to the Eu^{2+} 5d-bands in $Na_3Sc_2(PO_4)_3:Eu^{2+}$ phosphor, achieving zero TQ at 473 K.[7] Owing to energy compensation of a single-defect zinc vacancy, Li et al. reported that the emission intensity of a cyan phosphor $Ba_2ZnGe_2O_7:Bi^{3+}$ at 423 K was 114% of that at RT,[22] and its thermal stability was further improved after the introduction of oxygen vacancies by reductive atmosphere treatment. Qiu et al. reported that a deeper defect structure Tm_{Sr} formed by substituting Sr^{2+} with Tm^{3+} in $Sr_3SiO_5:Eu^{2+}$ led to zero TQ at 393 K.[23] In general, the more diverse and deeper the defects, the more carriers could be captured and the more energy could be transferred from the defects to luminescence centers.[14] However, the regulation and identification of defect types and levels are still under way, especially for multiple defects in phosphors. Moreover, the physical mechanism of defect-enhanced NTQ is still ambiguous. Therefore, the design and preparation for the NTQ materials with identified multiple defects remain a great challenge.

Here, we constructed three types of defect centers, including Ta vacancy (V_{Ta}^{5-}), Li substitution by Tb (Tb_{Li}^{2+}), and complex defects $(V_{Ta}Tb_{Li})^{3-}$ by introducing Tb^{3+} into a highly structurally rigid and defect-tunable $LiTaO_3$ matrix with the space group $R3c$ [Fig. 1(a)]. At 373 and 473 K, the fluorescence intensity is about 1.4 and 1.5 times that at 305 K, manifesting a wide temperature range NTQ [Figs. 1(b) and 1(c)]. As shown in Fig. 1(c), the thermal stability of $LiTaO_3:1\%Tb^{3+}$ at temperatures up to 473 K exceeds that of the existing commercial and advanced phosphor materials.[7] This NTQ is attributed to triple defects V_{Ta}^{5-}, Tb_{Li}^{2+}, and $(V_{Ta}Tb_{Li})^{3-}$ with trapping-depth-varied levels, as shown in Figs. 1(d)–1(f). They can effectively store charge carriers, thus acting as energy buffer layers in three consecutive temperature ranges of 305 to 373 K, 373 to 423 K and 423 to 473 K, respectively. Under thermal stimulation, the directional transport of the carriers from the defects to the activators can be continuously realized to compensate for the thermal loss from low to high temperatures, as depicted in Figs. 1(g)–1(i), thus achieving NTQ under a wide-range temperature. In other words, the luminescent source at high temperature originates from the Tb^{3+} itself and the supplement of the triple traps. This effect can compensate for the loss from the nonradiative processes and can thus suppress TQ. Triple defects have been confirmed by various advanced experimental techniques, including use of a high-resolution transmission electron microscope (HRTEM), positron annihilation lifetime spectroscopy (PALS), thermoluminescence (TL) spectroscopy, and first-principles theoretical calculations. Furthermore, $LiTaO_3:Tb^{3+}$ with triple defects-induced NTQ demonstrates broad application prospects in temperature-dependent anti-counterfeiting and optical information storage.

2 Materials and Methods

2.1 Synthesis of Phosphors

A series of $LiTaO_3:xTb^{3+}$ ($x = 0$, 0.5%, 1%, 2%) phosphors were synthesized by high-temperature solid-state reaction. The starting materials Li_2CO_3 (4N), Ta_2O_5 (4N), and activator Tb_4O_7 (4N) were used without further purification. The raw materials of phosphors activated by other elements (e.g., Eu) were also prepared using the corresponding oxides, such as Eu_2O_3 (4N). First, the stoichiometric amounts of raw materials were ground in a mortar with an appropriate amount of anhydrous ethanol for 30 min until the complete evaporation of ethanol. Then, the mixture was pre-sintered for 2 h at 600°C in a muffle furnace, cooled to RT, and fully ground. It was finally sintered at 1100°C for 5 h in air to obtain the phosphors.

2.2 Material Characterization

X-ray diffraction (XRD) patterns of the as-prepared phosphors were recorded on a Bruker D8 ADVANCE X-ray diffractometer with Cu K radiation ($\lambda = 0.15418$ nm). The composition and morphology of the powders were investigated on a JSM-6700F field emission scanning electron microscope as well as a JEM-2100F transmission electron microscope (Japan JEOL Corporation). X-ray absorption fine structure (XAFS) of Ta and Tb L_3 edge was obtained at Taiwan Light Source (BL17C1). XAFS data were processed using the Demeter XAS data processing package.[24] For the Ta L_3 edge, the data were fit in R-space, from 1 to 2.4 Å. Two Ta-O paths of varied lengths were used in the fitting. The R-space extended X-ray absorption fine structure (EXAFS) signal was obtained by a variable k^n-weighted Fourier transform ($n = 1, 2, 3$) of the EXAFS signal $\chi(k)$ over a k-range of 3 to 11.5 $Å^{-1}$. Photoluminescence (PL) and photoluminescence excitation (PLE) spectra were recorded by a Hitachi F-4600 fluorescence spectrophotometer with a 150 W xenon arc lamp as the light source. The temperature-dependent PL spectra were measured with TAP-02 high-temperature fluorescence test accessories. TL spectra were conducted by an SL008 TL meter (Radiation Science and Technology Co. Ltd, Guangzhou, China). UV irradiation for 5 min was used to charge the phosphor particles. Until the afterglow dissipated, the sample was heated to a certain temperature at a rate of 1 K/s to record the signals. X-ray photoelectron spectroscopy (XPS) measurements were performed by electron spectroscopy for a chemical analysis system (Axis Ultra, Kratos analytical-A Shimadzu Group company) with an Al (Mono) source (150 W). *In situ* temperature-dependent Raman characterization was performed using a Renishaw inVia Laser confocal Raman Spectrometer. The laser wavelength was 523 nm. Raman spectra were collected in the temperature range from 305 to 498 K.

In a PALS experiment, a ^{22}Na radioactive source was used as the positron source with a source intensity of about 13 μJ. Two identical samples were clamped on either side of a ^{22}Na source to form a typical sandwich geometry. The conventional positron annihilation lifetime spectrometer uses a pair of BaF_2 scintillators to detect gamma rays released after positron annihilation. The positron annihilation lifetime spectrum was collected by the fast-slow coincidence measurement technology. The total lifetime spectrum number is 2 million to ensure the validity of the statistics. The time resolution of the spectrometer was 195 ps, and the electronic plug-in of the measurement system was the standard NIM plug-in of EG&G Company.

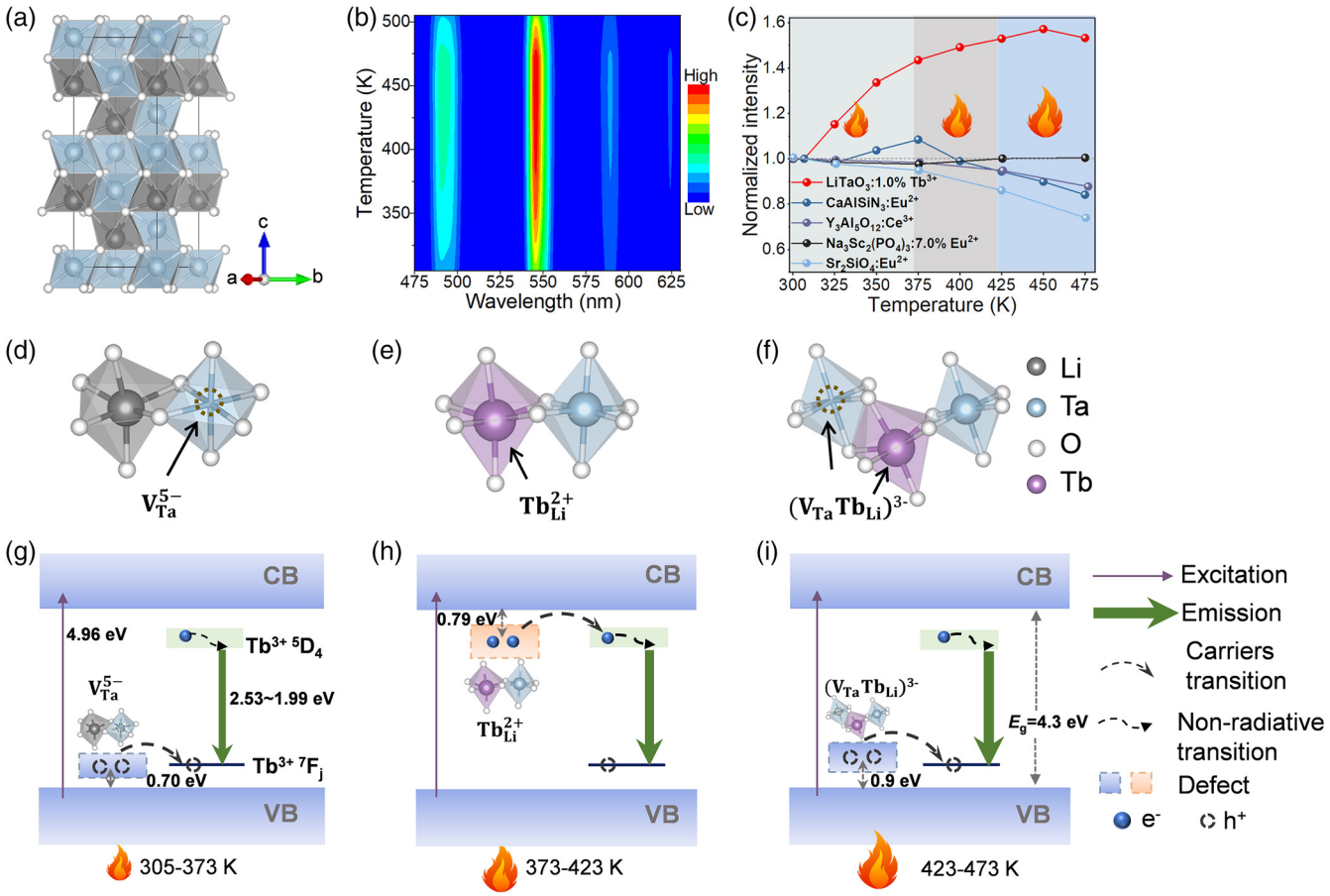

Fig. 1 NTQ performance and mechanism of $LiTaO_3:Tb^{3+}$ phosphor. (a) The crystal structure of $LiTaO_3$, where white, gray, and light blue spheres represent oxygen, Li in [LiO_6] octahedra, and Ta in [TaO_6] octahedra, respectively. These octahedra units are stacked closely together in the form of a co-triangular oxygen plane. (b) Temperature-dependent emission profile of $LiTaO_3:1\%Tb^{3+}$ under 250 nm excitation in the temperature range from 305 to 498 K. (c) Temperature-dependent normalized emission intensity of $LiTaO_3:1\%Tb^{3+}$ under 250 nm excitation in comparison to other commercial and advanced inorganic phosphors. Three color fillings represent three consecutive temperature zones: 305 to 373 K, 373 to 423 K, and 423 to 473 K, respectively. The results imply that $LiTaO_3:1.0\%Tb^{3+}$ shows relatively stable and increased emission in the working temperature range 373 to 473 K. (d)–(f) Schematic diagrams of triple gradient defects V_{Ta}^{5-}, Tb_{Li}^{2+}, and $(V_{Ta}Tb_{Li})^{3-}$, existing in $LiTaO_3:1\%Tb^{3+}$. (g)–(i) Schematic illustrations of triple defects-induced NTQ mechanisms. Triple defects with varied trapping depths could provide thermal increasing compensation in three consecutive temperature zones, thus achieving NTQ performance in a wide temperature range.

The performance of pressure sensing was studied by a laboratory-built integrated test system using a computer-controlled Shimadzu Universal stress testing instrument (AGS-X 10KN STD) with a photomultiplier tube (Hamamatsu photon, C13796) and a fluorescence spectrometer (SR-500I-B1-R, Andor).

2.3 Synthesis of Optical Information Storage Wafer

A certain amount of polydiethylsiloxane (PDMS) precursor and curing agent was put into a beaker, followed by adding phosphor particles with a phosphor/PDMS weight ratio of 0.4:1. After stirring evenly, the mixture was slowly poured into a 4 cm × 4 cm mold. A flexible wafer was obtained by heating and curing at 75°C for 1 h in an oven.

2.4 Preparation of Pressure Sensing Devices

The powder sample of $LiTaO_3:1\%Tb^{3+}$ was mixed with optical epoxy resin, followed by injection into a cylindrical mold container with a diameter of 20 mm and a height of 15 mm. After curing at 50°C for 6 h, the samples were taken from the mold. Before testing, the cured sample was exposed to UV radiation at 254 nm for 5 min.

2.5 DFT Theoretical Calculation

Theoretical calculation of the electronic structure was performed based on the density functional theory (DFT) implemented via the Vienna ab initio simulation package (VASP) code.[25] Moreover, the exchange correlation potential is selected by the

generalized gradient approximation (GGA) with the Perdew–Burke–Ernzerhof (PBE) formulation. The cutoff energy was 400 eV, and Brillouin zone integration was represented using the K-point sampling scheme of a $4 \times 4 \times 2$ Monkhorst–Pack grid. The stopping criterion for ionic optimization number is -0.03 Å^{-1}, while the criterion for allowed error in total energy is 1.0×10^{-6} eV. The formation energies (E_{for}) of $LiTaO_3$ with different defects were calculated by[26]

$$E_{for}[\text{defect}] = E_{tot}[\text{LiTaO}_3\text{-defect}] - E_{tot}[\text{LiTaO}_3] + \sum n_i \mu_i, \quad (1)$$

in which $E_{tot}(\text{LiTaO}_3\text{-defect})$ and $E_{tot}(\text{LiTaO}_3)$ represent the total energy of $LiTaO_3$ system with and without a defect, respectively. n_i represents the number of the removed ($n_i > 0$) or added ($n_i < 0$) i-type atoms, and μ_i is the chemical potential.

2.6 Calculation of Positron Annihilation Lifetime

Positron annihilation lifetime calculations were performed using an ABINIT software with two-component density-functional theory (TCDFT) calculations in the projector augmented-wave (PAW) framework. Calculations were performed using a $2 \times 2 \times 1$ $LiTaO_3$ supercell consisting of 120 atoms. In the defective structural models, a Ta vacancy (V_{Ta}^{5-}) was built by removing a Ta atom from the supercell, and a Tb atom was further applied to substitute a Li atom to form a complex-defect $(V_{Ta}Tb_{Li})^{3-}$.

3 Results

3.1 Structural Characterizations

The XRD patterns illustrate that all the as-prepared samples correspond well with standard $LiTaO_3$ hexagonal phase (PDF#29-0836) [Fig. 2(a) and Fig. S1 (see Supplementary Material)]. As shown in Fig. 2(b), the XRD Rietveld refinement of $LiTaO_3:1\%Tb^{3+}$ implies that the calculated data comply with the experimental measurements, where each Ta atom and Li atom are coordinated with six O atoms affording Ta-O and Li-O octahedron units (Table S1 in the Supplementary Material).[27–29] Moreover, the energy-dispersive X-ray spectroscopy (EDS) elemental mapping images show the uniform distribution of Ta, O, and Tb elements throughout phosphor particles of $LiTaO_3:Tb^{3+}$ [Fig. 2(c)].

The HRTEM images of $LiTaO_3:1\%Tb^{3+}$ indicate that the lattice fringe with d spacing of 0.372 nm corresponding to the (012) plane [Figs. 2(d)–2(e)] is well consistent with the refined structure of hexagonal phase $LiTaO_3$. Also, the selected area electron diffraction (SAED) pattern taken along the axis of $[2\bar{2}1]$ zone confirms the single-crystal nature of the phosphor particles [Fig. 2(f) panel (i)].[30] Figure 2(f) panels (ii)–(iv) show the filtered images of the regions within dashed white squares in Figs. 2(d) and 2(e). The atomic arrangement of Ta atoms observed from the images, as well as the recorded intensity profile verifies the phase of $LiTaO_3$ [L1–L5 in Fig. 2(f)], consistent with the XRD refinement result. The filtered images display that the lattice fringes are discontinuous, and some lattice positions are blurred or even missing, indicating the existence of defects [Fig. 2(f) panels (iii) and (iv) and Figs. S2, S3 in the Supplementary Material].[31] In contrast to the intensity profiles of perfect lattice L1, and L2/L3 with significant absence of Ta atoms (V_{Ta}^{5-}), Tb can be observed to occupy the position of Li atoms between the Ta atomic gap, forming the aliovalent substitution defects Tb_{Li}^{2+}, as shown in L4. Furthermore, since the ionic radius of Li^+ ($r = 0.76$ Å, CN $= 6$) is larger than that of Ta^{5+} ($r = 0.64$ Å, CN $= 6$), the doped Tb^{3+} ($r = 0.92$ Å, CN $= 6$) with a large radius is inclined to occupy the Li^+ lattice site. Also, the intensity distribution recorded along $L5$ verifies the existence of the complex defects $(V_{Ta}Tb_{Li})^{3-}$ composed of adjacent V_{Ta}^{5-} and Tb_{Li}^{2+}. These defects V_{Ta}^{5-}, Tb_{Li}^{2+}, and $(V_{Ta}Tb_{Li})^{3-}$ are expected as capture sites with different depths for storing carriers, compensating for the TQ effect, and thus increasing the emission intensity of $LiTaO_3:Tb^{3+}$ under high temperature.[7,32]

The formation of triple defects in $LiTaO_3:Tb^{3+}$ was also investigated from the thermodynamic point of view by first-principles calculations. The formation energies (E_{for}) of possible defects, including V_{Ta}^{5-}, Li vacancy (V_{Li}^{-}), inequivalence defects Tb_{Li}^{2+} and Tb_{Ta}^{2-}, as well as complex defects $(V_{Ta}Tb_{Li})^{3-}$ and $(V_{Li}Tb_{Li})^{+}$, are calculated as shown in Fig. S4 in the Supplementary Material. The results show that V_{Ta}^{5-}, Tb_{Li}^{2+}, and complex defect $(V_{Ta}Tb_{Li})^{3-}$ have lower formation energy than V_{Li}^{-}, Tb_{Ta}^{2-}, and $(V_{Li}Tb_{Li})^{+}$, also verifying the existence of triple defects V_{Ta}^{5-}, Tb_{Li}^{2+}, and $(V_{Ta}Tb_{Li})^{3-}$ as observed by HRTEM. Furthermore, the calculated energy band structures show that these defects have no significant effect on the bandgap (Fig. S5 in the Supplementary Material), but impact the electronic structure greatly. Density of states (DOS) of $LiTaO_3$ with these defects provides us with the specific effects of defects on the electronic structure [Figs. 2(h)–2(j)]. By comparing the total DOS profiles, $LiTaO_3$ with V_{Ta}^{5-} displays a higher occupied state at the bottom of the valence band (VB), leading to a better carrier storage capacity. It is evident that Tb_{Li}^{2+} can form a new intermediate level near the conduction band (CB). As an energy buffer layer, it is mainly composed of $Tb^{3+}4f$ orbitals, which can realize the ET from the defect level to the Tb^{3+} luminous level. Also, the presence of the complex defect $(V_{Ta}Tb_{Li})^{3-}$ has the same effect. A new intermediate level mainly consisting of $Tb^{3+}4f$ orbitals appears near the VB. This indicates that the complex defect can effectively improve the f-electron domination near the Fermi level, associated with the promoted carrier transfer.[33] All these characterizations confirm the existence of triple defects with varied electronic structures in $LiTaO_3:Tb^{3+}$, which could act as the energy buffer layers to promote NTQ.

3.2 NTQ Behaviors and Defect Identification of $LiTaO_3:Tb^{3+}$ Phosphor

To have a closer insight into the effect of defects on NTQ, TL, as one of the most effective techniques for characterizing the type and depth of defects,[34,35] was measured for the $LiTaO_3:1\%Tb^{3+}$ phosphor. The result demonstrates three successive temperature ranges of 300 to 373 K (T_1), 373 to 423 K (T_2), and 423 to 498 K (T_3), indicating three significant trap levels induced by triple defects associated with V_{Ta}^{5-}, Tb_{Li}^{2+}, and $(V_{Ta}Tb_{Li})^{3-}$, respectively [Fig. 3(a) and Figs. S6, S7 in the Supplementary Material]. This result is consistent with the aforementioned computational defect formation energy for these triple defects. The trap depths of defects were calculated using the following empirical equation[36]:

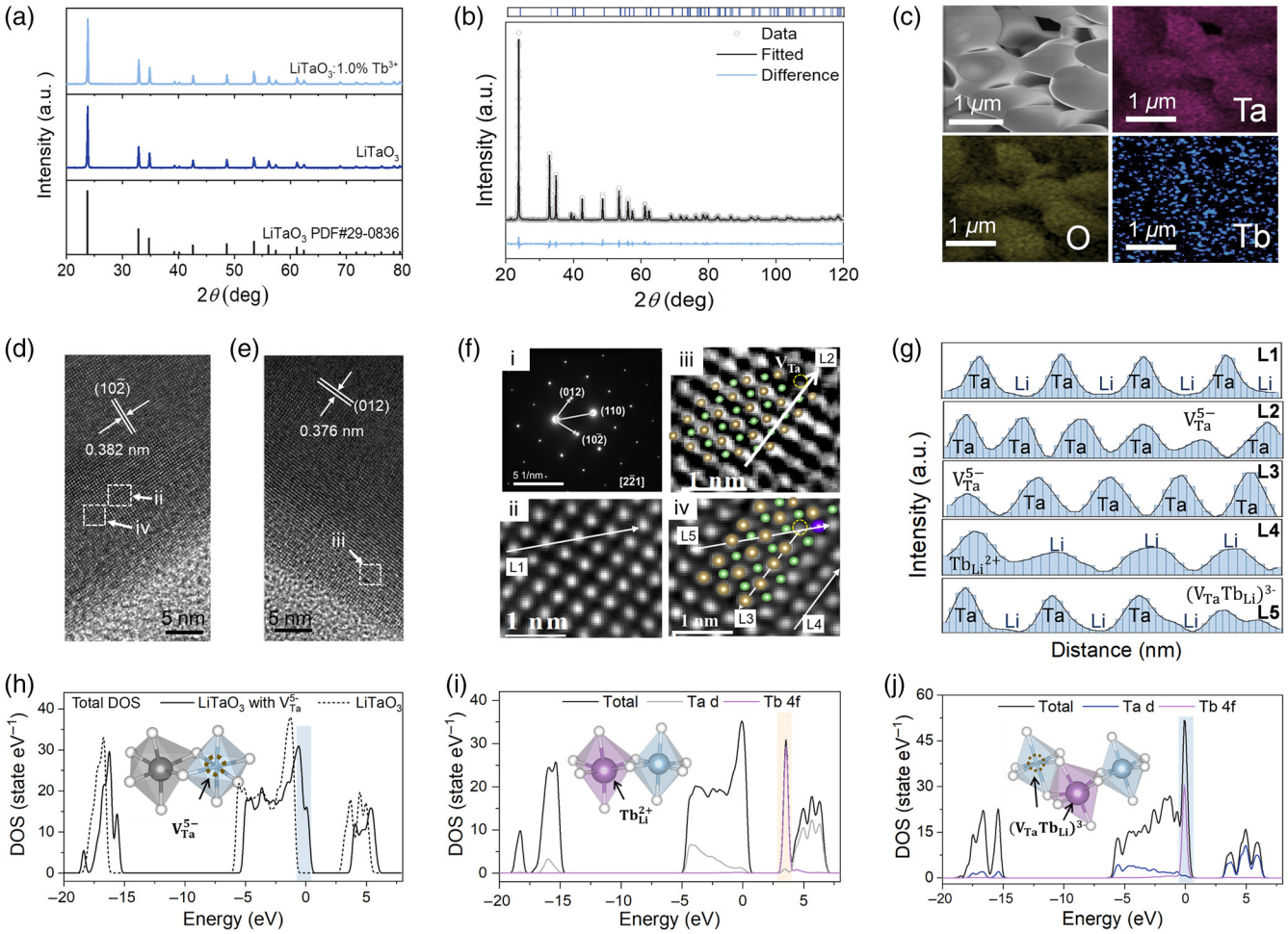

Fig. 2 Structural characterizations of $LiTaO_3:Tb^{3+}$ phosphor. (a) XRD patterns for $LiTaO_3:1\%Tb^{3+}$ and $LiTaO_3$. (b) XRD Rietveld refinement of $LiTaO_3:1\%Tb^{3+}$ with the measured and calculated data. (c) SEM and EDS mapping images of $LiTaO_3:Tb^{3+}$, implying the uniform doping of Tb throughout the whole particle. (d), and (e) HRTEM images of $LiTaO_3:1\%Tb^{3+}$. (f) SAED (i) and filtered images (ii–iv) of regions within dashed white squares in (d)–(e). (g) Intensity profiles along the L1–L5 lines recorded from (f) (ii–iv). The results confirm the existence of the V_{Ta}^{5-}, Tb_{Li}^{2+}, and $(V_{Ta}Tb_{Li})^{3-}$ defects in the lattice of $LiTaO_3:1\%Tb^{3+}$. (h)–(j) DFT calculations of $LiTaO_3$ with and without V_{Ta}^{5-}, Tb_{Li}^{2+}, and $(V_{Ta}Tb_{Li})^{3-}$ defects, where gray, light blue, white, and purple spheres represent Li, Ta, O, and Tb atoms, respectively. In (h), the solid line represents the total DOS for perfect lattice $LiTaO_3$, while the dotted line represents the total DOS for $LiTaO_3$ with V_{Ta}^{5-}.

$$E_{\text{trap}} = \frac{T_m}{500}, \tag{2}$$

where E_{trap} (eV) is the activation energy of trap level, and T_m (K) is the temperature at the TL peak. The calculated activation energies of these trap levels are 0.70, 0.79, and 0.90 eV, respectively [Fig. 3(b)]. Moreover, by increasing interval time after ceasing UV excitation, the intensity of T_1 shows a significant decrease in Fig. S8 in the Supplementary Material, while the deeper defects T_2 and T_3 are nearly unchanged. This further indicates that triple defects can function in different temperature zones, among which T_1 could be slowly released in an afterglow manner at low temperatures. Thus, these traps contribute to ET from the defect levels to the Tb^{3+}4f-band, which could explain the NTQ effect over a wide temperature range of 305 to 473 K.

To better elucidate how defects improve the NTQ performance of $LiTaO_3:Tb^{3+}$, the PALS combined with TCDFT calculation was performed to study the defect positron states, enabling the process of trapping and detrapping to be unambiguously established.[37–39] PALS is an effective means of identifying neutral or negatively charged vacancy-related defects in materials because it depends on the local structure of the defects enriched with positrons.[40,41] The experimental positron annihilation lifetime spectrum of $LiTaO_3:1\%Tb^{3+}$ was deconvolved to determine the components contributing to the positron state [Fig. 3(c)]. There are two dominant defect components τ_1 and τ_2 with lifetimes of 173.6 and 307.9 ps, contributing to the percentages of 54.7% and 42.4%, respectively. Moreover, the PALS of all samples with different Tb doping concentrations shows two similar deconvolved components (Fig. S9 and Table S2 in the

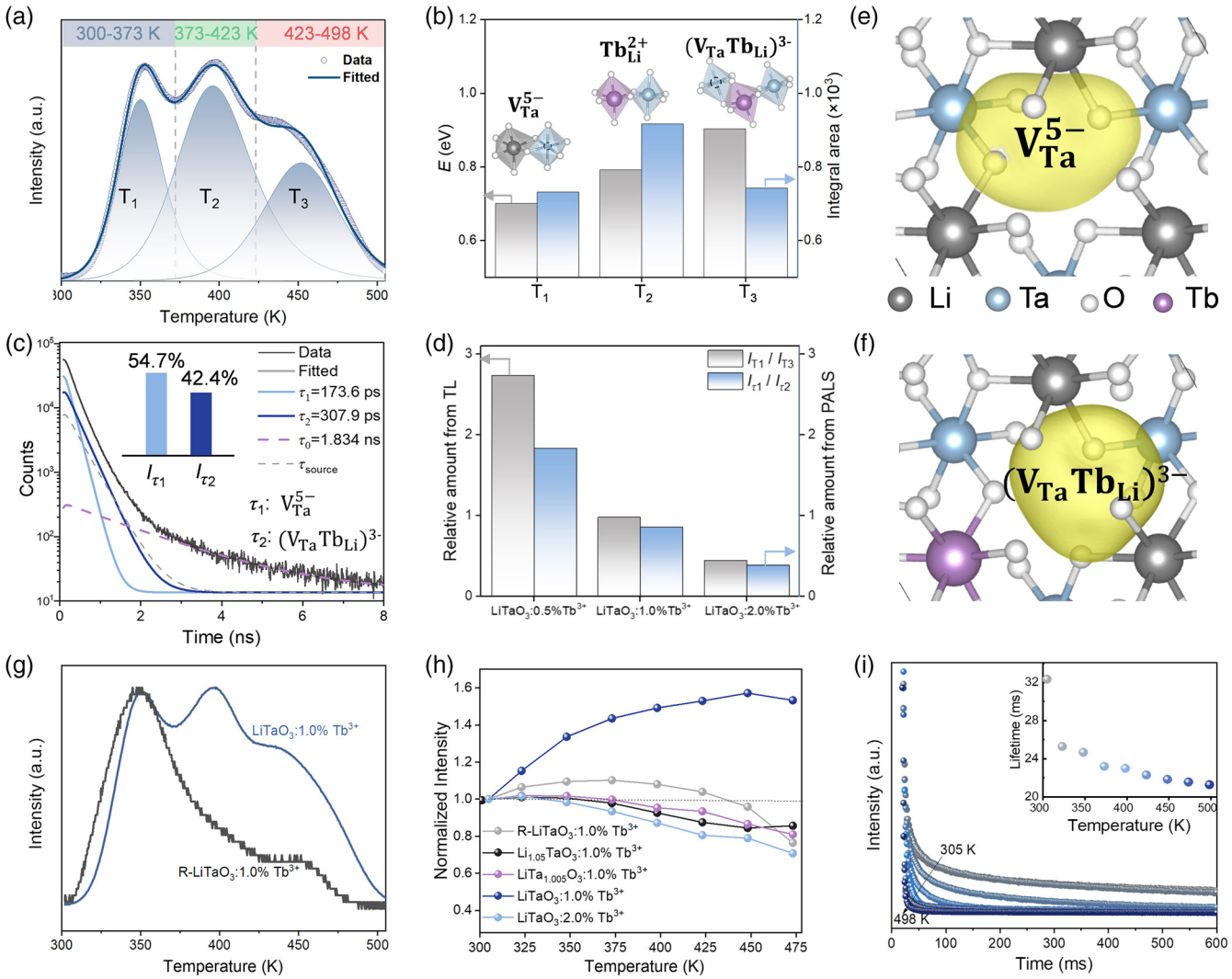

Fig. 3 Identification of defects in $LiTaO_3:Tb^{3+}$. (a) TL curve of $LiTaO_3:1\%Tb^{3+}$ with the fitted three peaks T_1, T_2, and T_3 in different temperature zones, corresponding to three defects, respectively. (b) The calculated trap depths and integral areas of three defects [V_{Ta}^{5-}, Tb_{Li}^{2+}, $(V_{Ta}Tb_{Li})^{3-}$]. (c) Experimental positron annihilation lifetime spectrum of $LiTaO_3:1\%Tb^{3+}$ with deconvolution fitting components. The results show two components, τ_1 and τ_2, ascribed to V_{Ta}^{5-} and $(V_{Ta}Tb_{Li})^{3-}$, respectively. The inset shows the percentages of the τ_1 and τ_2 components. (d) The relative ratios of two defects [V_{Ta}^{5-}, $(V_{Ta}Tb_{Li})^{3-}$] in $LiTaO_3:1\%Tb^{3+}$ with Tb^{3+} doping concentrations, obtained from the TL and PALS deconvolution results, respectively. (e) and (f) Positron density isosurface localized at V_{Ta}^{5-} and $(V_{Ta}Tb_{Li})^{3-}$ defects obtained using ABINIT. Yellow represents the positron accumulation. (g) TL curves of $LiTaO_3:1\%Tb^{3+}$ before and after reduction treatment at 1273 K for 2 h in mixed 95% Ar/5% H_2 atmosphere. (h) Comparison of thermal stability of different $LiTaO_3:Tb^{3+}$ samples. (i) PL decay curves of $LiTaO_3:1\%Tb^{3+}$ at increasing temperature from 305 to 498 K. These results provide sufficient evidence that triple defects with varied trapping depths in $LiTaO_3:1\%Tb^{3+}$ could promote NTQ performance in a wide temperature range.

Supplementary Material). The longest lifetime τ_0 is attributed to the pick-off annihilations of the ortho-positronium (o-Ps) in the free volume sites, present mainly in the amorphous regions of the polymer matrix. And it is not the main component obtained from the fit, occupying a very small fraction of 0.7% to 1.8%.

The corresponding positron state, including positron lifetime and density, was calculated using TCDFT with ABINIT, as shown in Table S3 in the Supplementary Material and Figs. 3(e) and 3(f). The calculated lifetime of $LiTaO_3$ with V_{Ta}^{5-} is 173.8 ps, which is close to the τ_1 component (173.6 ps) of the experimental results. Meanwhile, the $(V_{Ta}Tb_{Li})^{3-}$ lifetime is 299 ps. Thus, it is evident that the main positron lifetime components τ_1 and τ_2 can be attributed to V_{Ta}^{5-} and complex defect $(V_{Ta}Tb_{Li})^{3-}$, respectively. In addition, the τ_1 value is also consistent with the reported positron lifetime range (170 to 200 ps) of B-site vacancy in perovskite oxides ABO_3.[42–44] The relative percentage of two defects V_{Ta}^{5-} (T_1) and $(V_{Ta}Tb_{Li})^{3-}$ (T_3) obtained by TL spectra has the same trend as that obtained

by PALS [Fig. 3(d)], validating the existence of these two defects. Figures 3(e) and 3(f) clearly illustrate the positron density at the defects of V_{Ta}^{5-} and $(V_{Ta}Tb_{Li})^{3-}$. It is notable that the positron density in a perfect $LiTaO_3$ lattice is an order of magnitude lower than that in defects, as illustrated in Fig. S10 in the Supplementary Material. The high positron density caused by defects in the vicinity of the activator indicates that the negative charge defects, V_{Ta}^{5-} and $(V_{Ta}Tb_{Li})^{3-}$, have a strong ability to trap carriers, which could provide a source for ET from the defects to the 4f levels of Tb^{3+}.

To demonstrate the important role of triple defects in $LiTaO_3$:1%Tb^{3+} in promoting NTQ, a series of samples with regulatory defects were designed and prepared for comparison, including $LiTaO_3$:1%Tb^{3+} with reductive atmosphere treatment (R-$LiTaO_3$: 1%Tb^{3+}), Li or Ta excessive $Li_{1.005}TaO_3$: 1%Tb^{3+} or $LiTa_{1.005}O_3$: 1%Tb^{3+}, and Eu^{3+}, Tb^{3+} co-doped $LiTaO_3$ phosphor. The TL curve of R-$LiTaO_3$: 1%Tb^{3+} shows that the density of defects in T_1 remains unchanged, while those in T_2 and T_3 evidently decrease [Fig. 3(g)]. As expected, it shows weak NTQ in the low temperature range of 300 to 373 K, and TQ of PL emission can be detected as the temperature increases from 373 to 473 K [Fig. 3(h) and Fig. S11 in the Supplementary Material]. This is because the reducing atmosphere treatment increases the concentration of positively charged oxygen vacancy competing with the Tb_{Li}^{2+} defect, thus eliminating the effects of Tb_{Li}^{2+} and complex defect $(V_{Ta}Tb_{Li})^{3-}$. For the samples with excessive Li or Ta alone [Fig. 3(h)], the defect content in the samples decreased, thus leading to significant TQ.

By comparing Eu^{3+} single-doped and Eu^{3+}, Tb^{3+} co-doped $LiTaO_3$ phosphors (Fig. S12 in the Supplementary Material), the TL results imply that co-doping Tb significantly enhances the thermal stability of phosphors ascribed to rich defects in the co-doped materials. This further certifies that the defects play an important role in suppressing TQ. In agreement with previous reports,[45] upon increasing the temperature to 498 K, the PL dynamics in $LiTaO_3$: 1%Tb^{3+} is accelerated by ~35% [effective lifetime from $\tau(305\ \mathrm{K}) = 32.3$ ms to $\tau(373\ \mathrm{K}) = 21.3$ ms, Fig. 3(i)], suggesting that carrier trapping is strongly enhanced at high temperatures. The improved carrier separation and transfer efficiency were also verified by photoelectrochemical experiments. Figure S13 in the Supplementary Material illustrates that $LiTaO_3$: 1%Tb^{3+} has a larger current density and a smaller charge transfer resistance than $LiTaO_3$. It shows the photogenerated electron-hole separation under UV radiation is better for $LiTaO_3$: 1%Tb^{3+}.

3.3 Chemical Environments and Structures

Except for the defects effect, the chemical environments and intrinsic structures of $LiTaO_3$ and $LiTaO_3$: 1%Tb^{3+} were also evaluated. In the XPS spectra of Ta 4f [Fig. 4(a) and Fig. S14 in the Supplementary Material], $LiTaO_3$ shows the Ta $4f_{7/2}$ and

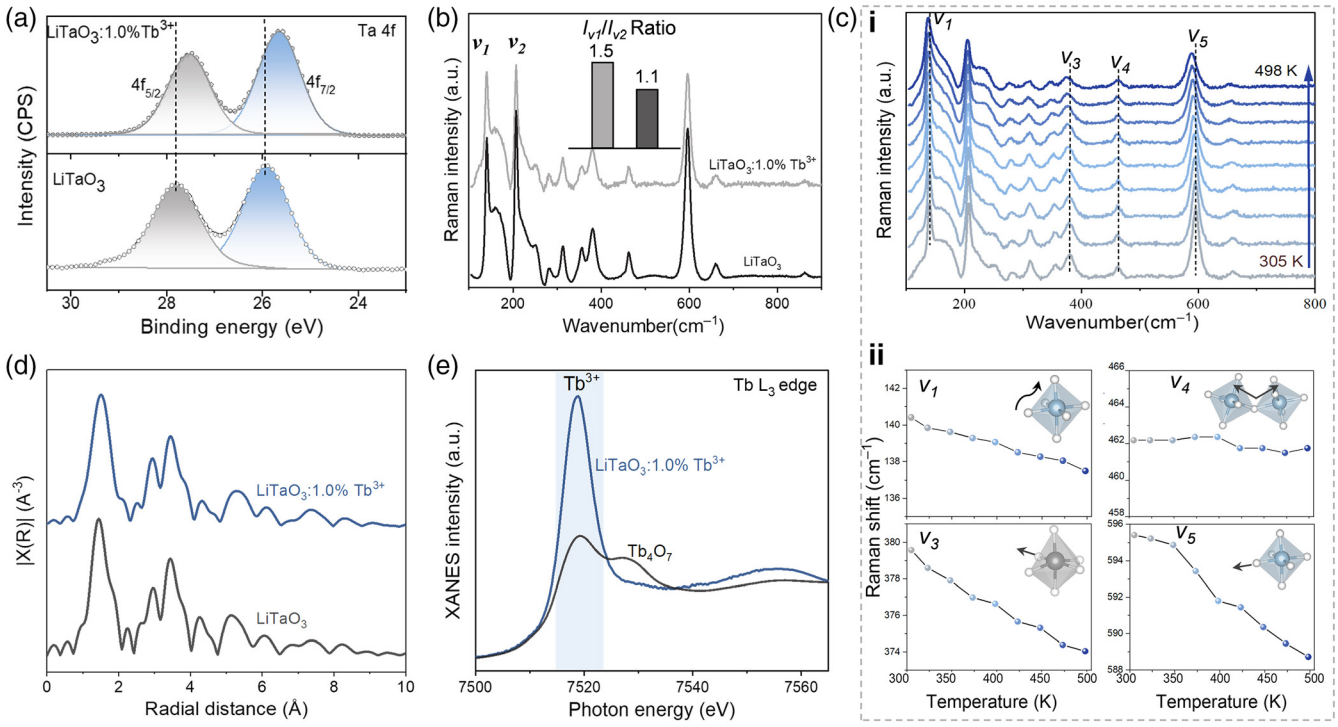

Fig. 4 Chemical environments and structures of $LiTaO_3$ and $LiTaO_3$: 1%Tb^{3+}. (a) High-resolution Ta 4f XPS spectra and (b) Raman spectra of $LiTaO_3$:1%Tb^{3+} and $LiTaO_3$. ν_1 and ν_2 stand for the modes of Ta-O framework deformation. The inset in (b) shows the integrated area ratios of ν_1/ν_2. (c) (i) Temperature-dependent *in situ* Raman spectra with the temperature range from 305 to 498 K, and (ii) Raman shifts of different modes with changing temperatures. ν_3, ν_4, and ν_5 represent Li–O stretching, O-Ta-O bending mode, and Ta-O stretching mode, respectively. (d) The EXAFS curves in R-space of $LiTaO_3$: 1%Tb^{3+} and $LiTaO_3$. (e) XANES spectra of the Tb L3 edge, recorded from $LiTaO_3$: 1%Tb^{3+} and Tb_4O_7 reference sample.

$4f_{5/2}$ peaks at 26.2 and 28.3 eV, respectively, confirming the dominant oxidation state of Ta^{5+}, whereas for $LiTaO_3$: 1%Tb^{3+}, these two peaks are shifted toward lower binding energy, which implies that the as-formed V_{Ta}^{5-} leads to a lower valence state.[46] In the Li 1s spectra (Fig. S15 in the Supplementary Material), $LiTaO_3$ exhibits the peaks locating at 55.16 eV. For $LiTaO_3$:1%Tb^{3+}, the peak position shifts toward lower binding energy of 54.92 eV. This results from partial occupation of the Li sites by low concentration of Tb^{3+}. Raman spectroscopy is an important tool for studying phonon patterns and assessing local structures in the NTQ materials.[3,47] As shown in Fig. 4(b), ν_1 and ν_2 represent the modes of Ta-O framework deformation.[48] The ratio of I_{ν_1}/I_{ν_2} increases from 1.1 to 1.5 when doping Tb^{3+}, indicating that the defects induce the change of the Ta-O deformation.[49]

In situ temperature-dependent Raman spectra are shown in Fig. 4(c). With the increase of temperature from 305 to 498 K, all Raman peaks become weaker in intensity and wider in shape, which is associated with the improvement of disordered or relaxation characteristics. There is a significant blueshift of the ν_1, ν_3, and ν_5 vibrational modes, providing a favorable pathway for thermal activation enhancement. The O-Ta-O bending mode at 462 cm^{-1} (ν_4) is strongly coupled with Li-O stretching (ν_3) and Ta-O stretching (ν_5). The O-Ta-O bending (ν_4) is almost constant with increasing temperature, suggesting that it could act as a structural buffer layer for thermally induced fluctuations to reduce thermal effects associated with the structural relaxation of the Tb^{3+} luminescent center. As the temperature increases, the phonon energy increases, and the ET from the defects to the luminescence energy level makes the lattice stable enough to suppress TQ. In addition, the reduction of the maximum phonon energy (662 cm^{-1}) may favor the luminescence of Tb^{3+} at high temperatures because the nonradiative relaxation could be effectively inhibited.[47]

The EXAFS data as well as the fitting results are shown in Fig. 4(d) and Fig. S16 and Table S4 in the Supplementary Material. The main peak at ≈ 1.96 Å is attributed to the scattering interaction between Ta and O atoms (Ta-O). And the average bond length of Ta-O increases from 1.967 to 1.973 Å with the increase of Tb doping concentration, suggesting that the lattice expands due to the substitution of Li^+ ($r = 0.76$ Å, CN = 6) by large radius Tb ions ($r = 0.92$ Å, CN = 6). Additionally, the increase of the coordination number of the Ta-O path further certifies the formation of defects in the material.[50] Furthermore, the local electronic structure of Tb was detected by X-ray absorption near-edge spectroscopy (XANES). Different from the mixed valence state of reference sample Tb_4O_7, the Tb^{3+} activator in $LiTaO_3$:1%Tb^{3+} is stabilized with the trivalent state [Fig. 4(e) and Fig. S17 in the Supplementary Material], which is similar to the Tb^{3+}-doped $NaLuF_4$ nanoscintillators.[16]

3.4 DFT Calculations

To deeply understand how the defect structures affect the NTQ performance of $LiTaO_3$:Tb^{3+}, DFT calculations were carried out by constructing $LiTaO_3$ models with these three defects. The structural models are shown in Figs. 5(a1)–5(a3). Differential charge density calculations [Figs. 5(b1)–5(b3) and 5(c1)– 5(c3)] reveal the depletion of electrons at the negative charge defect V_{Ta}^{5-} and the accumulation at the positive charge defect Tb_{Li}^{2+}. Moreover, there is a significant transfer of electrons from V_{Ta}^{5-} to Tb_{Li}^{2+} at the complex defect $(V_{Ta}Tb_{Li})^{3-}$. These results manifest that the accumulation and depletion of electrons at the defect sites are significantly increased. And the high electron/

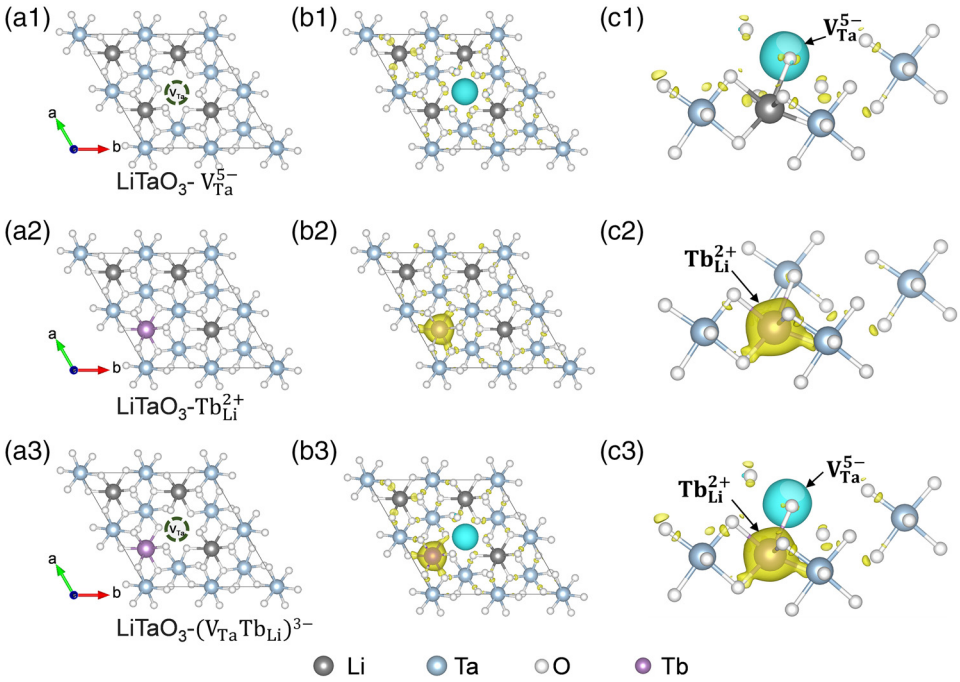

Fig. 5 DFT calculations of $LiTaO_3$-based defect systems. (a1)–(a3) Defect structure models of V_{Ta}^{5-}, Tb_{Li}^{2+} and $(V_{Ta}Tb_{Li})^{3-}$ in $LiTaO_3$. (b1)–(b3) (c1)–(c3) Charge density difference of $LiTaO_3$ with different defects. Yellow represents accumulation of electrons; cyan represents depletion of electrons.

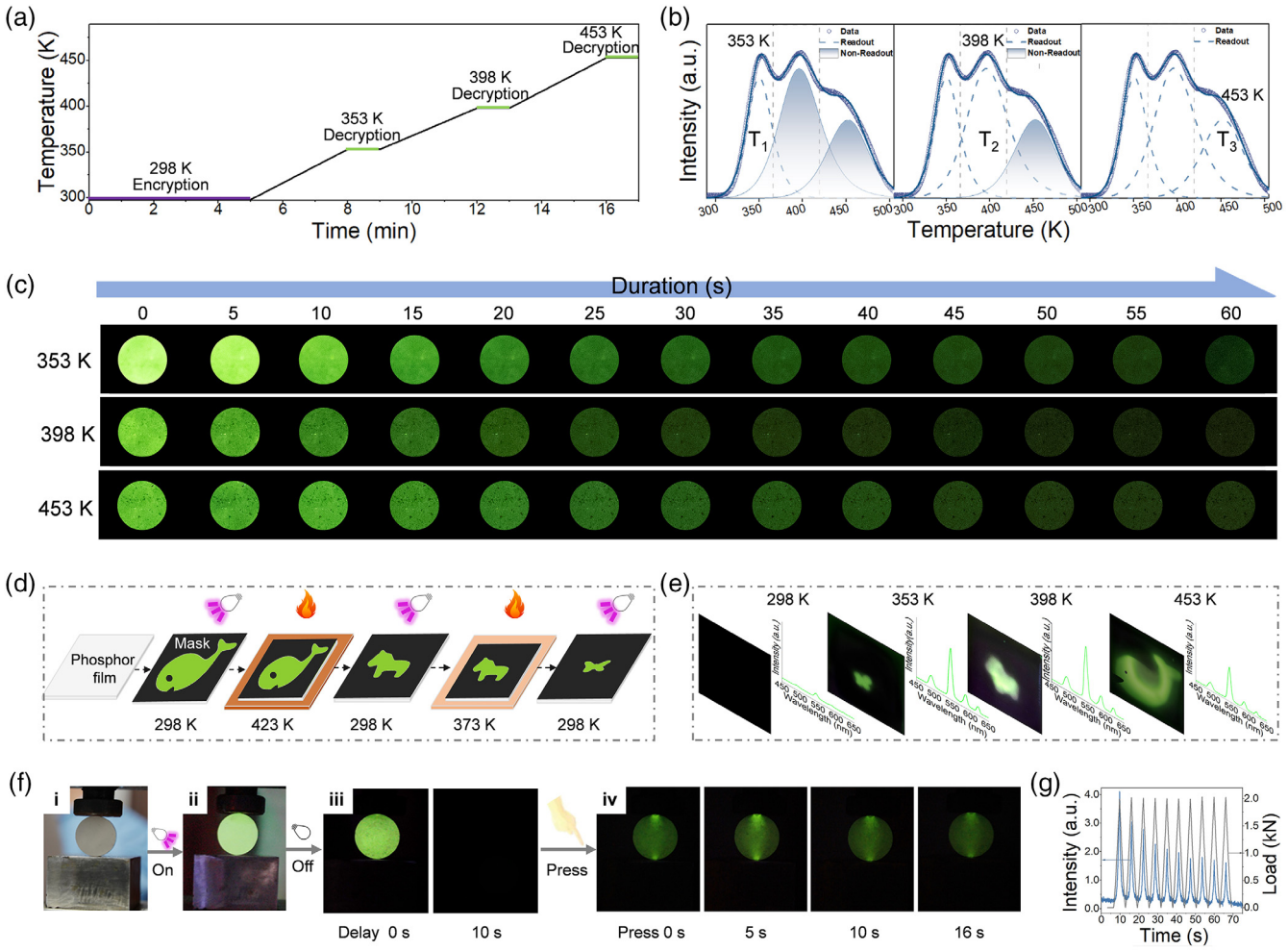

Fig. 6 Applications in temperature-dependent decryption, multiple-information storage, and pressure sensing. (a) Schematic diagram of temperature-dependent decrypting process. The information is encrypted by UV irradiation at 298 K. The rise of the temperature to 353 K results in a readout of T_1 defect-stored information. After cooling to 298 K, the further increase of temperature to 398 and 453 K successively could decrypt the information stored in T_2 and T_3 defects, respectively. (b) Schematic diagram of TL curves for temperature-dependent decrypting of triple defects. The dotted line indicates that the encrypted information in the defect is decrypted and read out at the corresponding temperature, and the blue filling represents that the information is still stably stored in the defect. (c) Temperature-dependent decrypting photos of a $LiTaO_3:1\%Tb^{3+}$ phosphor wafer with a diameter of 1 cm treated as the process in (a). After UV irradiation for 5 min, the wafer is heated up to 353, 398, and 453 K on a hot plate successively, and treatment at each temperature lasted for 60 s. The information is decoded by luminescence. (d) Schematic diagram of multiple information storage. The $LiTaO_3:1\%Tb^{3+}$ phosphor film is encrypted with the message whale under UV radiation with a mask, and then the charge carriers in the defect are partially emptied by heating at 423 K. The horse pattern is then written at 298 K and is partially emptied at 373 K for 30 s. Finally, encryption of the butterfly pattern was performed at RT. (e) The information pattern decrypted by heating and the corresponding spectrogram. At 298 K, the encrypted message is invisible. The butterfly pattern is decrypted at 353 K, and the horse and whale patterns could be read out at 398 and 453 K, respectively. (f) Schematic diagram of pressure sensing. The cylindrical sample is clipped in the fixture (i), and charged by UV light for 5 min (ii). After UV off and afterglow dissipation (iii), pressure was applied for 0, 5, 10 and 16 s, showing the corresponding pressure sensing images (iv). (g) The pressure sensing curve of intensity versus time obtained by cyclically applying a pressure of 2 kN after UV charging. This indicates that the information stored in the triple defects could be continuously decrypted by applying stress.

positron density in the defects facilitates the ET from the defects to the Tb^{3+} 4f orbital in the luminescence center at high temperatures.[51–53] Therefore, the abundant defects and smooth charge transfer confer the excellent NTQ properties of $LiTaO_3$:Tb^{3+}.

The proposed NTQ mechanism of Tb^{3+}-doped $LiTaO_3$ with triple defects is shown in Fig. S18 in the Supplementary Material. There are three types of defects that can capture carriers (electrons and holes) activated by UV light. The carriers in the defect could be decaptured to compensate for the heat loss upon thermal stimulation, thus achieving negative thermal quenching (NTQ) at high temperatures. Specifically, V_{Ta}^{5-} and $(V_{Ta}Tb_{Li})^{3-}$ act as hole traps (h-traps), while Tb_{Li}^{2+} acts as an electron trap. Under UV excitation, electrons and holes in the material could be separated, and holes in the VB are captured by the hole trap V_{Ta}^{5-} and $(V_{Ta}Tb_{Li})^{3-}$, and electrons in the CB are captured by the electron trap Tb_{Li}^{2+}, as shown in process (1). In the low-temperature region (300 to 373 K), holes in the shallowest trap V_{Ta}^{5-} are first decaptured to the luminescence centers (Tb^{3+}) [process (2)], and then holes and electrons recombine to generate luminescence [process (3)]. In the mid-temperature region (373 to 425 K), the electrons stored in the trap of Tb_{Li}^{2+} escape to the excited state level of Tb^{3+} and release energy in the form of luminescence. In the high-temperature region (425 to 475 K), the holes stored in the composite defect $(V_{Ta}Tb_{Li})^{3-}$ are released to compensate for the heat loss and thus lead to the NTQ behavior.

3.5 Applications in Temperature-dependent Information Encryption

Since the experimental and computational results indicate that multiple defect levels can trap and detrap optical energy, the $LiTaO_3:Tb^{3+}$ phosphor could be very suitable for applications in temperature-dependent information encryption and anti-counterfeiting. To demonstrate information storage capability mediated by triple defects with different trapping depths, we design a temperature-dependent decrypting algorithm, as shown in Fig. 6(a).

First, the optical information storage film consisting of $LiTaO_3:Tb^{3+}$ phosphor and PDMS was encrypted by UV light irradiation at 298 K. Then it was heated to three temperature zones in order to decrypt the information [Fig. 6(a)]. Figure 6(b) shows the TL curves of temperature-dependent decrypting with triple defects. The information decoding photos for the corresponding processes in Figs. 6(a) and 6(b) are shown in Fig. 6(c). The information was decrypted in the form of bright green light emission. At 353 K, the luminescence intensity changed from bright to dimming in 60 s, indicating that trap T_1 was emptied first. Upon being continuously heated to 398 and 453 K, the luminous intensity also shifted from bright to dim, manifesting that traps T_2 and T_3 were also emptied in order. Moreover, after each heating and de-trapping process, the use of UV charging can restore the carriers in the traps. By tailoring the heating duration from 0 to 80 s after UV charging, it can be clearly seen that under thermal stimulation, the stored charge carriers were released in the form of luminescence. The higher the temperature, the faster the charge carriers are released, and the shorter the duration of the thermally excited luminescence (Fig. S19 in the Supplementary Material).

Since the designed pattern information can be encrypted and decrypted intuitively, we also designed a pattern-based encoding method for multiple information encryption [Figs. 6(d) and 6(e) and Figs. S20 and S21 in the Supplementary Material]. First, the whale pattern information was encrypted into the phosphor film using UV light irradiation at 298 K [Fig. 6(d)], followed by a partial readout of the information at 423 K on a hot stage. After cooling to RT, the encryption of the horse pattern was performed and the partial information was emptied again at 373 K. After cooling, the butterfly pattern was encrypted by UV irradiation. The removed information for three patterns is not visible at RT. As the temperature increases from 353, 398, and 453 K, the encrypted patterns butterfly, horse, and whale could be decrypted sequentially [Fig. 6(e)]. The emission spectra at the corresponding temperatures were also recorded. Therefore, high-security and multidimensional information storage using $LiTaO_3:Tb^{3+}$ phosphor with trapping-depth-varied triple defects can be achieved by precisely controlling the heating temperature and encrypting different pattern information.

It is worth noting that the charge carriers stored in the defects also could be stimulated by pressure, which shows potential application of $LiTaO_3:Tb^{3+}$ phosphor in pressure sensing. Figure 6(f) demonstrates that the visual and continuous decryption of information can be achieved by applying pressure to an organic composite block made of $LiTaO_3:Tb^{3+}$ phosphor after 5 min of UV charging. The encrypted information was about 35% of its original intensity after 10 cycles of pressure loading, and the continuous luminescence could be observed by applying pressure onto the composite block [Fig. 6(g)]. Furthermore, the decryption of the information could also be achieved by a 980-nm laser (Fig. S22 in the Supplementary Material). The photo-stimulated luminescence spectrum is completely consistent with the emission spectra recorded under heating and stress, indicating that all this luminescence originates from Tb^{3+}. Therefore, the carriers in the defects could achieve a triple thermal, mechanical, and optical response, which provides a new strategy for developing temperature-dependent information encryption, multidimensional information storage, as well as press sensing.

4 Conclusion

In summary, triple defects V_{Ta}^{5-}, Tb_{Li}^{2+}, and $(V_{Ta}Tb_{Li})^{3-}$ with varied trapping depths, which were identified by HRTEM, PALS, TL, and first-principles calculations, have been constructed into a $LiTaO_3$ lattice by doping Tb^{3+}. The optimized $LiTaO_3:1\%Tb^{3+}$ phosphor exhibits a significant NTQ effect over a wide temperature range of up to 473 K, implying the potential applications in temperature-dependent anti-counterfeiting. The superior NTQ of $LiTaO_3:Tb^{3+}$ phosphor is mainly ascribed to triple defects V_{Ta}^{5-}, Tb_{Li}^{2+}, and $(V_{Ta}Tb_{Li})^{3-}$, which act as energy buffer layers to mitigate emission loss in three successive temperature zones, thus suppressing TQ in a wide temperature range. Furthermore, the multidimensional information encryption and decryption could be realized based on the temperature-dependent response behaviors of triple defects. This work opens a new avenue for the exploration of multiple defects-induced NTQ phosphors for high temperature and information-decrypting applications.

Acknowledgment

The authors acknowledge financial support from the National Key Research and Development Program of China (Grant No. 2018YFB0704103), the Natural Science Foundation of

Shanghai (Grant Nos. 22ZR1472100 and 20ZR1465900), the National Natural Science Foundation of China (Grant Nos. 92163117 and 62175210), the State Key Laboratory of ASIC & System (Grant No. 2020KF002), and the Innovation Project of Shanghai Institute of Ceramics (Grant No. E21ZC1770G). L. L. thanks the Taiwan Light Source for technical support. J. W. thanks the Program of Shanghai Academic Research Leader (Grant No. 20XD1424300) for financial support. The authors thank Professor Zhijun Zhang for providing valuable assistance in stress luminescence testing.

Data Availability

Additional data related to this study are available from the corresponding authors on reasonable request. Source data are provided with this paper.

References

1. M. Zhao et al., "Narrow-band emitters in LED backlights for liquid-crystal displays," *Mater. Today* **40**, 246–265 (2020).
2. M. Fang et al., "Evolutionary generation of phosphor materials and their progress in future applications for light-emitting diodes," *Chem. Rev.* **122**(13), 11474–11513 (2022).
3. J. Liao et al., "Thermally boosted upconversion and down-shifting luminescence in $Sc_2(MoO_4)_3$:Yb/Er with two-dimensional negative thermal expansion," *Nat. Commun.* **13**(1), 2090 (2022).
4. J. J. Joos et al., "Broadband infrared LEDs based on europium-to-terbium charge transfer luminescence," *Nat. Commun.* **11**(1), 3647 (2020).
5. S. Liu et al., "Wide range zero-thermal-quenching ultralong phosphorescence from zero-dimensional metal halide hybrids," *Nat. Commun.* **11**(1), 4649 (2020).
6. T. Hu et al., "Glass crystallization making red phosphor for high-power warm white lighting," *Light Sci. Appl.* **10**(1), 56 (2021).
7. Y. H. Kim et al., "A zero-thermal-quenching phosphor," *Nat. Mater.* **16**(5), 543–550 (2017).
8. H. Zhu et al., "Highly efficient non-rare-earth red emitting phosphor for warm white light-emitting diodes," *Nat. Commun.* **5**(1), 4312 (2014).
9. Y. Tang et al., "A multicolor-emitted phosphor for temperature sensing and multimode dynamic anti-counterfeiting," *J. Am. Ceram. Soc.* **105**(10), 6241–6251 (2022).
10. X. Zhang et al., "Abnormal thermal quenching effect of high power density excited fluorescent materials," *Chinese J. Lumin.* **42**(10), 1458–1481 (2021).
11. Y. Wei et al., "Strategies for designing antithermal-quenching red phosphors," *Adv. Sci.* **7**(8), 1903060 (2020).
12. X. Xu et al., "Advanced multi-laser-beam parallel heating system for rapid high temperature treatment," *J. Inorg. Mater.* **37**(1), 107–112 (2021).
13. G. Liu and Z. Xia, "Modulation of thermally stable photoluminescence in Cr^{3+}-based near-infrared phosphors," *J. Phys. Chem. Lett.* **13**(22), 5001–5008 (2022).
14. D. Wen et al., "Disorder–order conversion-induced enhancement of thermal stability of pyroxene near-infrared phosphors for light-emitting diodes," *Angew. Chem. Int. Ed.* **61**(28), e202204411 (2022).
15. Q. Liu et al., "Research progress on high throughput parallel synthesis of micro-nano powders libraries," *J. Inorg. Mater.* **36**(12), 1237–1246 (2021).
16. X. Ou et al., "High-resolution X-ray luminescence extension imaging," *Nature* **590**(7846), 410–415 (2021).
17. C. Wang et al., "Variation from zero to negative thermal quenching of phosphor with assistance of defect states," *Inorg. Chem.* **60**(24), 19365–19372 (2021).
18. M. Zhao et al., "Tailoring of white luminescence in a $NaLi_3SiO_4$:Eu^{2+} phosphor containing broad-band defect-induced charge-transfer emission," *Adv. Mater.* **33**(29), 2101428 (2021).
19. X. Zhou et al., "Multi-responsive deep-ultraviolet emission in praseodymium-doped phosphors for microbial sterilization," *Sci. China Mater.* **65**(4), 1103–1111 (2021).
20. Y. Li et al., "Long persistent phosphors—from fundamentals to applications," *Chem. Soc. Rev.* **45**(8), 2090–2136 (2016).
21. C. Cheng et al., "Designing high-performance LED phosphors by controlling the phase stability via a heterovalent substitution strategy," *Adv. Opt. Mater.* **8**(2), 1901608 (2020).
22. Y. Wei et al., "Anti-thermal-quenching Bi^{3+} luminescence in a cyan-emitting $Ba_2ZnGe_2O_7$:Bi phosphor based on zinc vacancy," *Laser Photonics Rev.* **15**(1), 2000048 (2021).
23. X. Fan et al., "Achieving long-term zero-thermal-quenching with the assistance of carriers from deep traps," *J. Mater. Chem. C* **6**(12), 2978–2982 (2018).
24. B. Ravel and M. Newville, "ATHENA, ARTEMIS, HEPHAESTUS: data analysis for X-ray absorption spectroscopy using IFEFFIT," *J. Synchrotron Radiat.* **12**(4), 537–541 (2005).
25. G. Kresse and J. Furthmüller, "Efficiency of ab-initio total energy calculations for metals and semiconductors using a plane-wave basis set," *Comput. Mater. Sci.* **6**(1), 15–50 (1996).
26. S. Shen et al., "Highly active Si sites enabled by negative valent Ru for electrocatalytic hydrogen evolution in LaRuSi," *Angew. Chem. Int. Ed.* **61**(32), e202206460 (2022).
27. R. Hu et al., "Synergistic defect engineering and microstructure tuning in lithium tantalate for high-contrast mechanoluminescence of Bi^{3+}: toward application for optical information display," *Mater. Chem. Front.* **5**(18), 6891–6903 (2021).
28. R. Hu et al., "UV–Vis-NIR broadband-photostimulated luminescence of $LiTaO_3$:Bi^{3+} long-persistent phosphor and the optical storage properties," *Chem. Eng. J.* **392**, 124807 (2020).
29. M. Nikl et al., "Emission and storage properties of $LiTaO_3$:Tb^{3+} phosphor," *J. Appl. Phys.* **79**(6), 2853–2856 (1996).
30. M. Zhao et al., "Li substituent tuning of LED phosphors with enhanced efficiency, tunable photoluminescence, and improved thermal stability," *Sci. Adv.* **5**(1), eaav0363 (2019).
31. L. Zhang et al., "Sodium-decorated amorphous/crystalline RuO_2 with rich oxygen vacancies: a robust pH-universal oxygen evolution electrocatalyst," *Angew. Chem. Int. Ed.* **60**(34), 18821–18829 (2021).
32. G. Liu et al., "Cation-assisted formation of porous TiO_{2-x} nanoboxes with high grain boundary density as efficient electrocatalysts for lithium–oxygen batteries," *ACS Catal.* **8**(3), 1720–1727 (2018).
33. J. Zhang et al., "Single platinum atoms immobilized on an MXene as an efficient catalyst for the hydrogen evolution reaction," *Nat. Catal.* **1**(12), 985–992 (2018).
34. M. Deng et al., "Novel co-doped Y_2GeO_5:Pr^{3+},Tb^{3+}: deep trap level formation and analog binary optical storage with submicron information points," *Adv. Opt. Mater.* **9**(10), 2002090 (2021).
35. X. Wang et al., "Solar-blind ultraviolet-C persistent luminescence phosphors," *Nat. Commun.* **11**(1), 2040 (2020).
36. K. Van den Eeckhout et al., "Revealing trap depth distributions in persistent phosphors," *Phys. Rev. B* **87**(4), 045126 (2013).
37. D. J. Keeble et al., "Identification of lead vacancy defects in lead halide perovskites," *Nat. Commun.* **12**(1), 5566 (2021).
38. J. Wiktor et al., "Positron annihilation spectroscopy investigation of vacancy clusters in silicon carbide: combining experiments and electronic structure calculations," *Phys. Rev. B* **89**(15), 155203 (2014).
39. J. Wiktor et al., "Two-component density functional theory within the projector augmented-wave approach: accurate and self-consistent computations of positron lifetimes and momentum distributions," *Phys. Rev. B* **92**(12), 125113 (2015).
40. F. Tuomisto and I. Makkonen, "Defect identification in semiconductors with positron annihilation: experiment and theory," *Rev. Mod. Phys.* **85**(4), 1583–1631 (2013).

41. X. Ning et al., "Modification of source contribution in PALS by simulation using Geant4 code," *Nucl. Instrum. Methods Phys. Res. Sect. B* **397**, 75–81 (2017).
42. D. J. Keeble et al., "Identification of A- and B-site cation vacancy defects in perovskite oxide thin films," *Phys. Rev. Lett.* **105**(22), 226102 (2010).
43. D. J. Keeble et al., "Cation vacancies in ferroelectric $PbTiO_3$ and $Pb(Zr,Ti)O_3$: a positron annihilation lifetime spectroscopy study," *Phys. Rev. B* **76**(14), 144109 (2007).
44. H. Ouhbi and J. Wiktor, "Polaron formation and hopping in tantalate perovskite oxides: $NaTaO_3$ and $KTaO_3$," *Phys. Rev. B* **104**(23), 235158 (2021).
45. M. Liu et al., "Suppression of temperature quenching in perovskite nanocrystals for efficient and thermally stable light-emitting diodes," *Nat. Photonics* **15**(5), 379–385 (2021).
46. Z. Zhang et al., "Tantalum-based electrocatalyst for polysulfide catalysis and retention for high-performance lithium-sulfur batteries," *Matter* **3**(3), 920–934 (2020).
47. H. Yuan et al., "Understanding negative thermal expansion of Zn_2GeO_4 through local structure and vibrational dynamics," *Inorg. Chem.* **60**(3), 1499–1505 (2021).
48. F. X. Zhang et al., "Ion irradiation induced strain and structural changes in $LiTaO_3$ perovskite," *J. Phys. Condens. Matter* **33**(18), 185402 (2021).
49. M. Si et al., "Local electric-field-driven fast Li diffusion kinetics at the piezoelectric $LiTaO_3$ modified Li-rich cathode–electrolyte interphase," *Adv. Sci.* **7**(3), 1902538 (2020).
50. E. Song et al., "Mn^{2+}-activated dual-wavelength emitting materials toward wearable optical fibre temperature sensor," *Nat. Commun.* **13**(1), 2166 (2022).
51. C. Linderälv et al., "Luminescence quenching via deep defect states: a recombination pathway via oxygen vacancies in Ce-doped YAG," *Chem. Mater.* **33**(1), 73–80 (2021).
52. Z. Li et al., "Spin engineering of single-site metal catalysts," *Innovation* **3**(4), 100268 (2022).
53. Z. Zhi et al., "Facile synthesis of zinc indium oxide nanofibers distributed with low content of silver for superior antibacterial activity," *Small Struct.* 2200291 (2023).

Mingxue Deng is a research intern at Shanghai Institute of Ceramics, Chinese Academy of Sciences (SICCAS). She received her BS degree from Northeastern University in 2018, and MS degree from SICCAS in 2021. Her main research interest concentrates on designing rare earth optical functional materials via high-throughput methods for optical storage, high power lighting and sterilization applications.

Xingzhong Cao is currently a full professor at Institute of High Energy Physics (IHEP), Chinese Academy Sciences. He received his PhD degree from Lanzhou University, China, in 2004. Before joining IHEP in 2010, he worked at KEK and Kyoto University of Japan for four years. His research interests include the technical development of positron annihilation spectroscopy and slow positron beam, and their application for the characterization of lattice defects in solid materials and the study of internal relationships between the macroscopic properties of materials and atomic scale microscopic defect structures.

Zhenzhen Zhou is an associate professor at Shanghai Institute of Ceramics, Chinese Academy of Sciences (SICCAS). She graduated from Hebei Normal University with BS and MS degrees in 2008 and 2011, respectively, and received her PhD degree from SICCAS in 2019. She has worked at SICCAS since 2011, mainly engaged in the research of high-throughput experimental methodology, fluorescent materials, scintillation materials, and other optical functional materials and devices.

Jiacheng Wang is currently a full professor of functional materials at Shanghai Institute of Ceramics, Chinese Academy of Sciences (SICCAS). He obtained his PhD from SICCAS in 2007. Before getting back to SICCAS in 2013, he spent six years on functional materials research at the University of Tokyo (collaborator: Prof. Makoto Onaka), Dresden University of Technology (collaborator: Prof. Stefan Kaskel), and Cardiff University (collaborator: Prof. Graham Hutchings). He was an Alexander von Humboldt Fellow, JSPS Postdoctoral Fellow for Foreign Researcher, and Marie Curie Intra-European Fellow. His present research focuses on rational design and preparation of advanced functional materials for energy transformation and photoluminescence.

Qian Liu is a full professor at Shanghai Institute of Ceramics, Chinese Academy of Sciences. She received BS and MS degrees from Tianjin University in 1982 and 1987, respectively, and a PhD degree from Shanghai Institute of Ceramics, Chinese Academy of Sciences, in 1994. Her research interests are the application of high-throughput technology for the rapid discovery and preferential selection of new materials and material systems, including luminescent materials, dielectric materials, steel materials, etc.

Biographies of the other authors are not available.